Dyes and Pigments 113 (2015) 210–218

Contents lists available at ScienceDirect

Dyes and Pigments

journal homepage: www.elsevier.com/locate/dyepig

Solution-processed interlayer of discotic-based small molecules for organic photovoltaic devices: Enhancement of both the open-circuit voltage and the fill factor

Ho Jun Song [a, b], Eui Jin Lee [a], Doo Hun Kim [a], Tae Ho Lee [a], Munju Goh [c], Sangkug Lee [b], Doo Kyung Moon [a, *]

[a] Department of Materials Chemistry and Engineering, Konkuk University, 1 Hwayang-dong, Gwangjin-gu, Seoul 143-701, Republic of Korea
[b] Cungcheong Regional Division IT Convergence Material R&D Group, Korea Institute of Industrial Technology, 89 Yangdaegiro-gil, Ipjang-myeon, Seobuk-gu, Cheonan-si, Chungcheongnam-do 331-822, Republic of Korea
[c] Carbon Convergence Materials Research Center, Korea Institute of Science and Technology, Eunhari san 101, Bongdong-eup, Wanju-gun, Jeonbuk 565-905, Republic of Korea

ARTICLE INFO

Article history:
Received 20 May 2014
Received in revised form
8 August 2014
Accepted 10 August 2014
Available online 19 August 2014

Keywords:
Small molecule
OPVs
Interlayer
DLC
CPEs
Semiconductor

ABSTRACT

A novel alcohol/water-soluble, discotic type derivative of pyrene was obtained using a simple synthesis process. The pyrene derivative was dissolved in organic solvents and highly polar solvents. The absorption spectrum of the pyrene derivative in a thin film was almost identical with that observed in solution compared with a fluorene derived co-polymer, the extensive planarity of the pyrene unit is invoked to rationalize this observation. According to an XRD measurement, a huge portion of the pyrene derivatives are arranged face-on in regard of the substrate due to their discotic structure. A photovoltaic device containing the pyrene derivative exhibited an open-circuit voltage of 0.73 V, current density of 14.6 mA/cm^2, fill factor of 65.1% and a power conversion efficiency of 7.0%. The photovoltaic device with the pyrene derivative exhibited an improved fill factor compared with that of the fluorene co-polymer (60.7%) due to the discotic structure. An inverted photovoltaic device containing pyrene derivative showed a power conversion efficiency of 8.3%.

1. Introduction

Conjugated polymers have been widely used in organic light emitting diodes (OLEDs) [1–4], organic photovoltaic cells (OPVs) [5–11] and organic thin film transistors (OTFTs) [12,13] for several decades. For some times, OPVs have drawn crucial concern for these applications due to the universal technology tendency toward economic potential and continuative growth coupled with efforts to preserve the environment. However, the poor power conversion efficiency (PCE) of these materials has been the greatest barrier in organic photovoltaic development [6].

The next ideal conditions must be achieved in OPV materials and devices to improve the PCE [8]: 1) increase of the short-circuit current (J_{SC}) through a wide absorption spectrum, 2) rise of the open-circuit voltage (V_{OC}) through optimization of the highest occupied molecular orbital (HOMO) and lowest unoccupied molecular orbital (LUMO) energy levels, and 3) improve the fill factor (FF) by controlling resistance at the interfaces. To achieve these ideal conditions, various efforts continue to be applied to control the materials of the active layer and the device structure: various donor–acceptor (D–A) type polymers, additives, thermal treatments, and film thicknesses. However, there is still an inevitable loss at the interfaces because of the charge transport barriers between the active layer and the metal cathode [14].

To improve the charge transport between the interfaces, a number of investigations to study the effects of introducing an interlayer have been reported recently. In particular, most research efforts have focused on alcohol/water soluble conjugated polymer electrolytes (CPEs) for the interlayer. The Maes group recently reported that the PCE improved from 3.8% to 6.6% with imidazolium-substituted polythiophene used as the CPE [15]. In the Cao group, a PCE of 8.3% was reported with a device structure that introduced poly[(9,9-bis(30-(*N*,*N*-dimethylamino)propyl)-2,7-fluorene)-alt-2,7-(9,9-dioctylfluorene)] (PFN) between the active layer and the cathode, and an inverted device configuration with PFN improved the PCE to 9.2%, with increases of the J_{SC}, V_{OC}, and FF [16,17]. It has

* Corresponding author. Tel.: +82 2 450 3498; fax: +82 2 444 0765.
E-mail address: dkmoon@konkuk.ac.kr (D.K. Moon).

http://dx.doi.org/10.1016/j.dyepig.2014.08.007
0143-7208/

been suggested that these interlayers introduce an enhanced built-in potential across the device because of the presence of an interface dipole, which is conducive to a refinement in the charge-transport, an elimination of the built-up space charge, and a diminution in the recombination losses of the charge carriers [14,16].

Small molecules have various advantages compared with polymers, such as straightforward synthesis and purification, monodispersity and precise structures, residual end functionality and good reproducibility [18,19]. A number of research studies on active materials by small molecules have been reported [20–22], but only a few investigations of interlayers about small molecules by solution-process have been reported in the field of OLEDs and OPVs [4,23].

In this study, we synthesized novel alcohol/water-soluble discotic type small molecules. The discotic derivatives exhibit unique material properties, such as effective charge-carrier mobilities by one-dimensional structure and anisotropic mechanical and optical properties [13,24,25]. Discotic liquid crystal (DLC) materials with effective charge carrier mobility along columnar phases have the possibility to be used as the active constituent in electronic applications. Moreover the adjustment of their molecular packing and large fraction orientation exhibits a principal factor for the performance of devices due to the design of the molecular structure [26].

Thus, we synthesized 3,3′,3″,3‴-((pyrene-1,3,6,8-tetrayltetrakis(benzene-4,1-diyl))tetrakis(oxy))tetrakis(*N*,*N*-dimethylpropan-1-amine) (PBPA) using a simple synthesis process, as shown in Scheme 1. The dimethyl-amine derivative was introduced as the end group of the pyrene derivative to provide good alcohol/water-solubility. Due to their molecular packing and long-range organization, improved FF and V_{OC} values are expected in OPVs using these discotic type pyrene derivatives.

2. Experimental section

2.1. Instruments and characterization

Unless otherwise specified, all reactions were performed under a nitrogen atmosphere. The solvents were dried using the standard procedures. All column chromatography was performed with silica gel (230–400 mesh, Merck) as the stationary phase. ^{1}H NMR spectra were collected by a Bruker ARX 400 spectrometer using solutions in $CDCl_3$ with chemical concentrations recorded in ppm units using TMS as the internal standard. The elemental analyses were measured with an EA1112 apparatus using a CE Instrument. The electronic absorption spectra were measured in chloroform using an HP Agilent 8453 UV–Vis spectrophotometer. The cyclic voltammetric waves were obtained using a Zahner IM6eX electrochemical workstation with a 0.1 M acetonitrile (purged with nitrogen for 20 min) solution containing tetrabutyl ammonium hexafluorophosphate (Bu_4NPF_6) as the electrolyte at a constant scan rate of 50 mV/s. ITO, a Pt wire, and silver/silver chloride [Ag in 0.1 M KCl] were used as the working, counter, and reference electrodes, respectively. The electrochemical potential was calibrated against Fc/Fc^+. The HOMO levels of the polymers were determined using the oxidation onset value. The onset potentials are the values obtained from the intersection of the two tangents drawn at the rising current and the baseline changing current of the CV curves. TGA measurements were performed on a NETZSCH TG 209 F3 thermogravimetric analyzer. Differential scanning calorimetry (DSC) was used to determine phase-transition temperatures on a Netzsch DSC 200 F3 maia differential scanning calorimeter with a constant heating/cooling rate of 10 °C/min. Texture observations by polarizing optical microscopy (POM) were made with a Leica DM2500M and DFC295. All GPC analyses were performed using THF as an eluent and a polystyrene standard as a reference. Grazing Incidence X-ray diffraction (GIXD) patterns were obtained using a SmartLab 3 kW (40 kV 30 mA, Cu target, wavelength: 1.541871 Å) instrument of Rigaku, Japan. Topographic images of the active layers were obtained through atomic force microscopy (AFM) in a tapping mode under ambient conditions using an XE-100 instrument. Scanning Kelvin probe microscopy (SKPM) measurements were carried out on AFM equipment, using the standard SKPM mode. Theoretical analyses were performed using density functional theory (DFT), as approximated by the B3 LYP functional and employing the 6-31G* basis set in Gaussian09. The contact angle measurements were performed using a Kruss DSA100. SEM microscopy was performed on a JEOL model JSM-6701F field-emission scanning electron microscope operating at 10 kV. The melting point was evaluated using a Carl Zeiss AXIO IMAGER MIM polarizing optical microscope (POM) equipped with a Linkam TH-600PM and L-600 heating and cooling stage with temperature control.

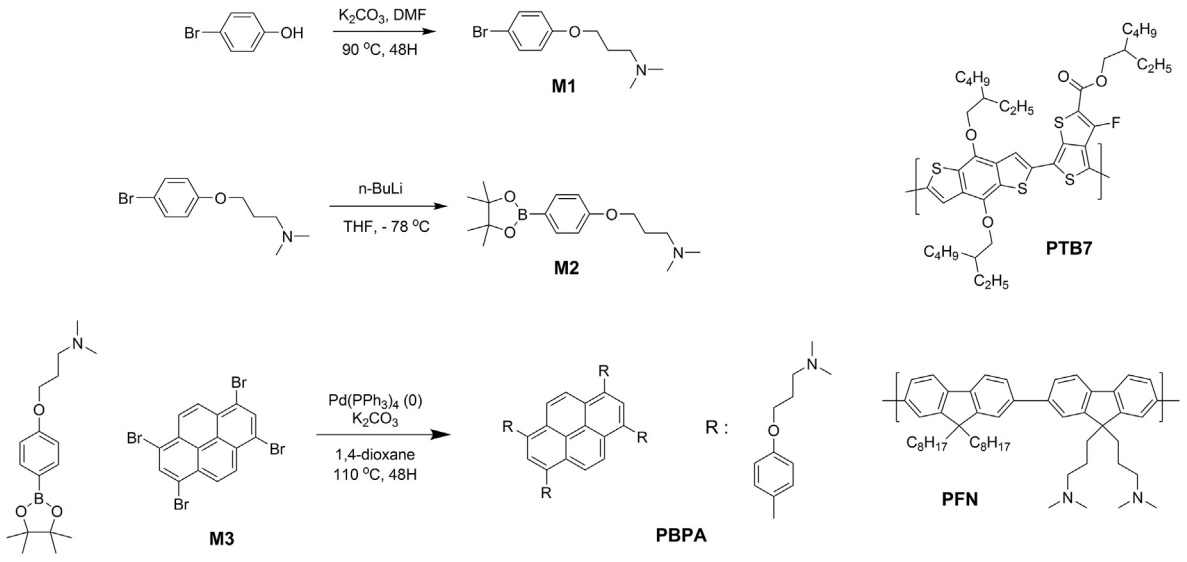

Scheme 1. Synthesis route of PBPA and chemical structure of PTB7, PFN.

2.2. Fabrication and characterization of polymer solar cells

All of the bulk-heterojunction PV cells were prepared using the following device fabrication procedure. The glass/indium tin oxide (ITO) substrates [Sanyo, Japan (10 Ω/γ)] were sequentially lithographically patterned, cleaned with detergent, and ultrasonicated in deionized water, acetone, and isopropyl alcohol. The substrates were then dried on a hot plate at 120 °C for 10 min and treated with oxygen plasma for 10 min to improve the contact angle immediately before the film coating process. Poly(3,4-ethylenedioxythiophene): poly(styrenesulfonate) (PEDOT:PSS, Baytron P 4083 Bayer AG) was passed through a 0.45-μm filter before being deposited onto the ITO substrates at a thickness of ca. 32 nm by spin-coating at 4000 rpm in air and then dried at 120 °C for 20 min inside a glove box. Composite solutions with polymers and PCBM were prepared using chlorobenzene (CB) with 1,8-diiodooctane (DIO). The concentration was adequately controlled in the 0.3–0.5 wt% range. The solutions were then filtered through a 0.45-μm PTFE filter and spin-coated (500–2000 rpm, 30 s) on top of the PEDOT:PSS layer. The PFN solution in methanol and acetic acid was spin-coated on the top of the obtained active layer at 4000 rpm for 30 s to form a thin interlayer of 8–10 nm. The device fabrication was completed by depositing thin layers of Al (200 nm) at pressures of less than 10^{-6} torr. The active area of the devices was 4.0 mm^2. Finally, the cell was encapsulated using a UV-curing glue (Nagase, Japan). In this study, all of the devices were fabricated with the following structure: ITO glass/PEDOT:PSS/polymer:PCBM/with or without interlayer/Al/encapsulation glass; ITO glass/ZnO/with or without interlayer/polymer:PCBM/MoO_3/Ag/encapsulation glass.

The illumination intensity used to test the OPVs was calibrated using a standard a Si photodiode detector that was equipped with a KG-5filter. The output photocurrent was adjusted to match the photocurrent of the Si reference cell to obtain a power density of 100 mW/cm^2. After the encapsulation, all of the devices were operated under an ambient atmosphere at 25 °C. The current–voltage (I–V) curves of the photovoltaic devices were measured using a computer-controlled Keithley 2400 source measurement unit (SMU) that was equipped with a Peccell solar simulator under an illumination of AM 1.5G (100 mW/cm^2). The thicknesses of the thin films were measured using elipsometer of Elli-SE=Uam12.

The hole-only devices were fabricated with a diode configuration of ITO (170 nm)/PEDOT:PSS (40 nm)/PTB7:$PC_{71}BM$ (50 nm)/interlayer/MoO_3 (30 nm)/Al (100 nm). The hole mobility of the active layers was calculated from the SCLC using the *J–V* curves of the hole-only devices in the dark as follows:

$$J = \frac{9}{8}\varepsilon_r\varepsilon_0\mu_{h(e)}\frac{V^2}{L^3}\exp\left(0.89\sqrt{\frac{V}{E_0 L}}\right)$$

where ε_0 is the permittivity of free space (8.85×10^{-14} C/V cm); ε_r is the dielectric constant (assumed to be 3, which is a typical value for conjugated polymers) of the polymer; $\mu_{h(e)}$ is the zero-field mobility of holes (electrons); L is the film thickness; and $V = V_{appl} - (V_r + V_{bi})$, where V_{appl} is the applied voltage to the device, V_r is the voltage drop due to series resistance across the electrodes, and V_{bi} is the built-in voltage.

2.3. Materials

All reagents were purchased from Aldrich, Acros or TCI companies. All chemicals were used without further purification. PTB7 and PFN were purchased from Nano clean tech (Product NO.: OS0737, OS0743). The following compounds were synthesized following modified literature procedures: 1,3,6,8-tetrabromopyrene (M3) [20].

2.3.1. 3-(4-Bromophenoxy)-N,N-dimethylpropan-1-amine (***M1***)

4-Bromophenol (10 g, 57.8 mmol), 3-dimethylaminopropylchloride hydrochloride (27.4 g, 173.4 mmol), K_2CO_3 (23.9 g, 173.4 mmol) were placed in a round-bottomed flask, and under a nitrogen atmosphere and dry DMF (20 mL) was added. The mixture was placed in a microwave reactor and heated to 90 °C using 300 W of microwave power for 4 h. After reaction quenching, the reaction mixture was purified by column chromatography on silica gel (dichloromethane as eluent) to obtain the product as light-yellow oil (6.1 g, yield: 40.8%). ^{1}H NMR (400 MHz; $CDCl_3$; Me_4Si): δ = 7.32 (d, 2H, J = 8.8 Hz), 6.74 (d, 2H, J = 8.8 Hz), 3.94 (t, 2H, J = 6.4 Hz), 2.41 (t, 2H, J = 6.8 Hz), 2.23 (s, 6H), 1.92 (m, 2H, J = 6.8 Hz). ^{13}C NMR (100 MHz; $CDCl_3$; Me_4Si): 158.12; 132.15; 116.28; 112.62; 66.39; 56.26; 45.52; 27.46. Anal. Calcd for: $C_{11}H_{16}BrNO$: C, 51.18; H, 6.25; N, 5.43. Found: C, 48.06; H, 5.90; N, 6.01. IR (KBr, cm^{-1}): 2946, 2861, 2766, 1590, 1488, 1285, 1241, 641.

2.3.2. N,N-dimethyl-3-(4-(4,4,5,5-tetramethyl-1,3,2-dioxaborolan-2-yl)phenoxy)propan-1-amine (***M2***)

To a 100-mL flame-dried two necked flask was added M1 (3.0 g, 11.6 mmol) and freshly distilled THF (80 mL). The resulting solution was cooled at −78 °C and 8.7 mL n-butyllithium (13.9 mmol, 1.6 M in hexane) was added over 10 min under a nitrogen atmosphere. The mixture was stirred at −78 °C for 1 h. 2-Isopropoxy-4,4,5,5-tetramethyl-1,3,2-dioxaborolane (2.6 g, 13.9 mmol) was added rapidly to the solution, and the resulting mixture was slowly warmed to room temperature for 24 h. The mixture was poured into 50 mL water and extracted with $CHCl_3$ (300 mL). The combined organic layers were washed with brine and dried over anhydrous $MgSO_4$. The solvent was removed by rotary evaporation, and the residue purified by column chromatography on silica gel (ethylacetate:dichloromethane as eluent) to obtain the product as a light-yellow oil (1.6 g, yield: 45.0%). ^{1}H NMR (400 MHz; $CDCl_3$; Me_4Si): δ = 7.77 (d, 2H, J = 8.8 Hz), 6.90 (d, 2H, J = 8.8 Hz), 3.94 (t, 2H, J = 6.4 Hz), 2.46 (t, 2H, J = 6.8 Hz), 2.26 (s, 6H), 1.88 (m, 2H, J = 6.8 Hz) 1.25 (s, 12H). ^{13}C NMR (100 MHz; $CDCl_3$; Me_4Si): 161.57; 136.73; 113.41; 83.13; 74.40; 66.02; 54.09; 45.42; 27.43; 25.00. Anal. Calcd for: $C_{17}H_{28}BNO_3$: C, 66.90; H, 9.25; N, 4.59. Found: C, 66.73; H, 9.23; N, 4.63. IR (KBr, cm^{-1}): 2981, 2936, 2816, 2716, 1566, 1463, 1281, 1245.

2.3.3. 3,3′,3″,3‴-((Pyrene-1,3,6,8-tetrayltetrakis(benzene-4,1-diyl))tetrakis(oxy))tetrakis(N,N-dimethylpropan-1-amine) (PBPA)

M2 (1.60 g, 5.24 mmol), 1,3,6,8-tetrabromopyrene (M3) (0.30 g, 0.87 mmol) and $Pd(PPh_3)_4(0)$ (0.35 g, 0.30 mmol), were placed in a Schlenk tube, purged with three nitrogen/vacuum cycles, and under nitrogen atmosphere added 2 M degassed aqueous K_2CO_3 (15 mL) and dry 1,4-dioxane(30 mL). The mixture was heated to 90 °C and stirred in the dark for 48 h. After reaction quenching, the mixture was poured into 50 mL water and extracted with $CHCl_3$ (100 mL). The combined organic layers were washed with brine and dried over anhydrous $MgSO_4$. The solvent was removed by rotary evaporation, and the final product was obtained after drying in vacuum. Off-white solid. (0.25 g, yield: 31.5%) ^{1}H NMR (400 MHz; $CDCl_3$; Me_4Si): δ = 8.15 (s, 1H), 7.94 (s, 4H), 7.57 (d, 8H, J = 8.8 Hz), 7.07 (d, 8H, J = 8.8 Hz), 4.12 (t, 8H, J = 6.4 Hz), 2.51 (t, 8H, J = 6.8 Hz), 2.29 (s, 24H), 2.02 (m, 8H, J = 6.8 Hz). ^{13}C NMR (100 MHz; $CDCl_3$; Me_4Si): 158.66; 136.97; 133.69; 132.27; 131.89; 129.83; 128.21; 126.35; 125.31; 114.63; 66.61; 56.70; 45.80; 27.88. Anal. Calcd for: $C_{60}H_{70}N_4O_4$: C, 79.09; H, 7.74; N, 6.15. Found: C, 76.94; H, 7.42; N, 4.90. IR (KBr, cm^{-1}): 2944, 2857, 2814, 2762, 1513, 1494, 1458, 1285, 1244. Melting point: 192 °C.

3. Results and discussion

3.1. Synthesis and thermal properties

Scheme 1 exhibits the chemical structures of the materials and the synthesis process. As shown in Scheme 1, M1 was synthesized by the Williamson ether reaction under microwave heating, and M2 was synthesized using M1 and a boronic ester. Finally, PBPA was synthesized by a Suzuki-coupling reaction with monomer M2 and 1,3,6,8-tetrabromopyrene. The reaction mixture to form PBPA was heated for 48 h at 110 °C with a palladium(0) catalysts, a 2 M potassium carbonate solution in 1,4-dioxane as a solvent. The synthesized M3 was purified using several rounds of re-crystallization with methanol/H_2O, and the yield of PBPA was 31%. The obtained PBPA was soluble in organic solvents (chlorobenzene, orthodichlorobenzene, chloroform) and highly polar solvents (methanol, ethanol).

The solubility of PBPA and PFN, a representative alcohol/water soluble polymer was compared. We added acetic acid in MeOH to improve solubility relative to protonation of the terminal dimethylamino groups. For the same weight ratio condition (5 mg of material/cosolvent (Acetic acid 10 μL + MeOH 2.5 mL)), PFN was soluble with heat treatment, but PBPA completely dissolved without heat treatment at RT (See Fig. S3). Thus, PBPA exhibited higher solubility in highly polar solvents compared with PFN. Using a PBPA solution, a uniform and transparent film was formed by spin-coating.

Fig. 1a) shows the thermal properties of the PBPA. PBPA experienced a 5% weight loss at a temperature of 358 °C, indicating high thermal stability due to the rigid pyrene structure. This result was similar with the thermal stability of a conjugated polymer, which makes PBPA applicable to OLED and OPVs which demand a thermal stability above 300 °C [6]. We investigated the thermal phenomenon using differential scanning calorimetry (DSC) and polarizing optical microscope (POM) analyses (Fig. 1b)). The DSC trace of the PBPA revealed no obvious liquid-crystal phase transitions and exhibited only melting to an isotropic phase upon heating at 192 °C, which is consistent with the POM result. Interestingly, in the crystal phase at RT, PBPA formed large plate domains, which might be due to the formation of a columnar phase by the discotic pyrene derivative (POM and SEM image of Fig. 1b)).

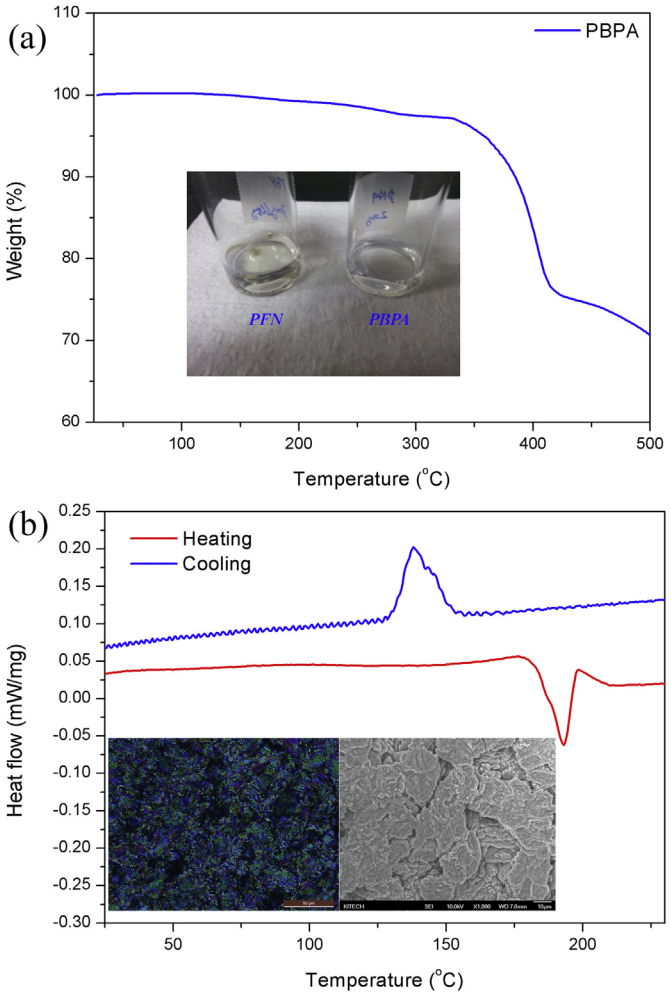

Fig. 1. a) TGA graph of PBPA (inset: solubility test of PBPA and PFN for 5 mg of material/cosolvent (Acetic acid 10 μL + MeOH 2.5 mL)) b) DSC trace of PBPA (inset: polarized optical micrograph (left) and scanning electron microscope (right) of PBPA cooling form the isotropic phase at 200 °C).

3.2. Optical and electrochemical properties

Fig. 2a) shows the UV–visible spectra of PBPA and PFN. The maximum absorption spectra of PBPA (λ_{max}) were exhibited at 387 nm in solution (10^{-5} M in a co-solvent of acetic acid and methanol) and at 384 nm in the thin film form. Especially, the absorption spectrum of PBPA in its thin film form almost matched up with that of solution, which means that the more planar pyrene unit effectively decreases the steric hindrance in the thin film and facilitates stronger association in solution [27]. The maximum absorption of PFN (λ_{max}) were exhibited at 387 nm in solution (10^{-5} M in cosolvent of acetic acid and methanol) and at 392 nm in the thin film form. In thin film form, the absorption spectrum of PFN also exhibited a broad spectrum in the section of 400–425 nm, which significantly differed from that of PBPA. This broad spectral absorption is the result of the decrease in the dihedral angle between fluorene derivatives in the thin film due to the stronger interdigitate interactions [28]. The calculated optical band gaps of PBPA and PFN by the measured value of UV onset for the film were 2.96 and 2.89 eV, respectively.

Fig. 3 exhibits the cyclic voltammograms of PBPA and PFN. The cyclic voltammograms were recorded in 0.1 M tetrabutylammonium-hexafluorophosphate acetonitrile solution. As shown in Fig. 3, the PBPA and PFN exhibited typical p-type oxidation peaks. The oxidation (E_{ox}^{onset}) of PBPA and PFN occurred at +0.93 V and 1.24 V, and the HOMO energy levels of PBPA and PFN determined through calculation were −5.26 eV and −5.57 eV, respectively. The LUMO energy levels were obtained from the gap between the HOMO energy levels and the optical band gap energies. As a result, the LUMO levels of PBPA and PFN were −2.29 and −2.68 eV, respectively. As shown in Fig. 3b), the HOMO level of PBPA (−5.26 eV) is similar with that of PEDOT:PSS (−5.0 eV).

3.3. XRD analysis and DFT calculation

Fig. 4 exhibits the X-ray diffraction investigation of the films of PBPA and PFN to analyze their ordering structures. The samples for measurement were fabricated to the structure of spin-casted film on the surface of a Si-wafer using solution with acetic acid and MeOH. In the out-of-plane diffraction pattern of PBPA, as shown in Fig. 4a), a prominent diffraction peak showed at 18.7°, which indicates an out-of-plane peak (010) due to the arrangement of a regular columnar structure by π–π stacking. The π–π stacking distance of PBPA was 0.48 nm ($\lambda = 2d\sin\theta$). This π–π stacking distance matched up with the stacking distance among the pyrene units by formation of hexagonal columnar phase reported in the

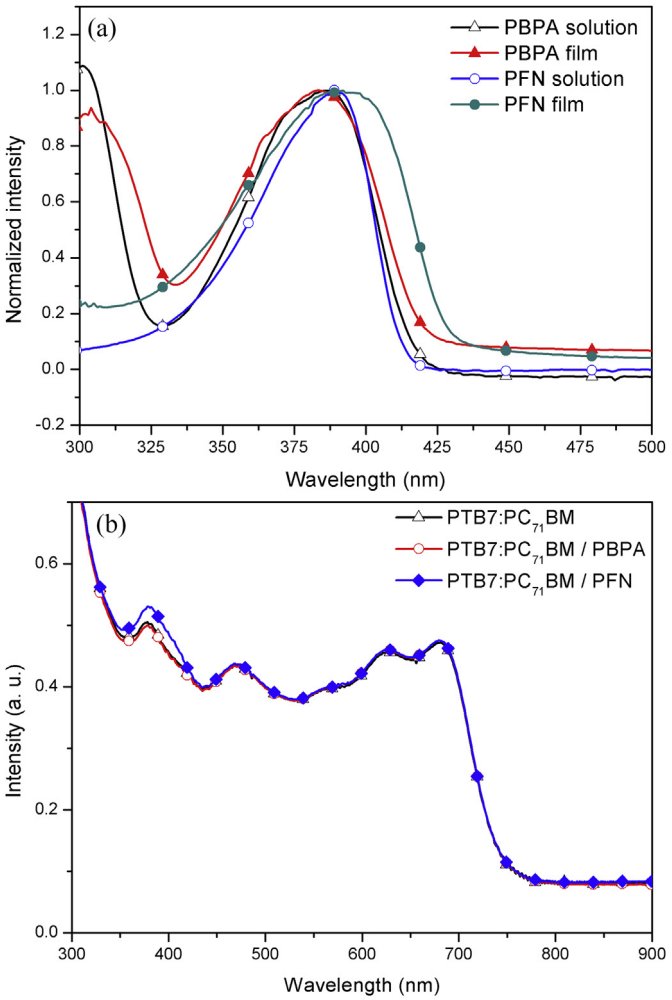

Fig. 2. Absorption spectra for a) PBPA and PFN in solution & thin film b) spin-coated layers of PBPA and PFN on the top of the active layer (PTB7:$PC_{71}BM$).

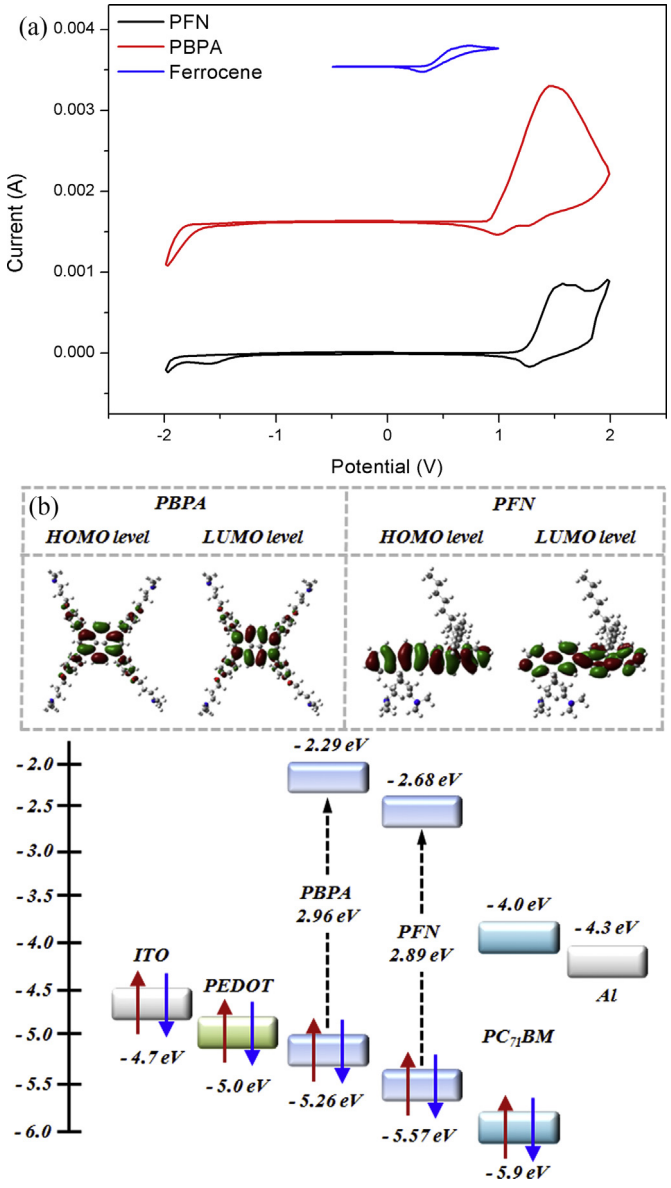

Fig. 3. a) Cyclic voltammogram of PBPA and PFN b) DFT Gaussian simulation and band diagram of PBPA, PFN, ITO, $PC_{71}BM$, Al.

literature of pyrene-based molecules [24,29]. In contrast, in the out-of-plane diffraction pattern of PFN, a very weak diffraction peak was observed at 19.3°, which means (010) diffraction corresponding to π–π stacking. The π–π stacking distance of PFN was 0.46 nm. The results of PBPA and PFN were comparable with the results for the π–π stacking distance of fluorene–benzene (d_π = 4.0–4.4 Å) [30]. However, the diffraction peak of PBPA was sharper compared with that of PFN, which indicates PBPA exhibited a more strongly ordered orientation than that of PFN.

In the in-plane diffraction pattern of PBPA, as shown in Fig. 4b), a diffraction pattern was rarely exhibited. When considering the results of the out-of-plane and in-plane diffraction for PBPA, these results suggest that a huge fraction of the PBPA derivatives exhibit face-on orientation in regard of the substrate; namely, the π-stacking orientation is perpendicular to the substrate direction [5,31]. The ordered orientation and oriented face-on structure of PBPA reduce the series resistance in the electron transport direction for OPVs, which may result in the improved FF in the PBPA-based OPV device compared with that of the PFN-based OPV device (see Table 1).

By calculating PBPA and PFN using a DFT calculation, the torsion angle was comparatively analyzed. For PBPA, the torsion angle between pyrene and benzene was 53–57°, while the torsion angle between fluorene derivatives for PFN was 37°. Compared with PBPA, the formation of a planar backbone was observed for PFN (see SI). However, as shown in the XRD results, the π–π stacking distances of PBPA (0.48 nm) and PFN (0.46 nm) exhibited similar values. Namely, the torsion angle of PBPA is 20° higher than that of PFN, but the π–π stacking distances were similar. These results suggest that PBPA exhibited effective π–π stacking due to the staggered stacking of PBPA [13].

3.4. Characterization of OPV devices

Fig. 5 and Table 2 exhibit the data for devise performance. Each device was fabricated as follows: ITO (170 nm)/PEDOT:PSS (40 nm)/active layer (50–80 nm)/Interlayer (~5 nm)/Al (100 nm). The donor polymer in the active layer was thieno[3,4-*b*]-thiophene-benzodithiophene (PTB7), and the acceptor derivative in the active layer was phenyl-C71-butyric acid methyl ester ($PC_{71}BM$). The blend ratio for PTB7/$PC_{71}BM$ was 1:1.5 by weight, and the active layer was spin-coated from a mixed solvent (chlorobenzene 97 vol%, 1,8-diiodoctane 3 vol%). On the top of the active layer, either a PBPA

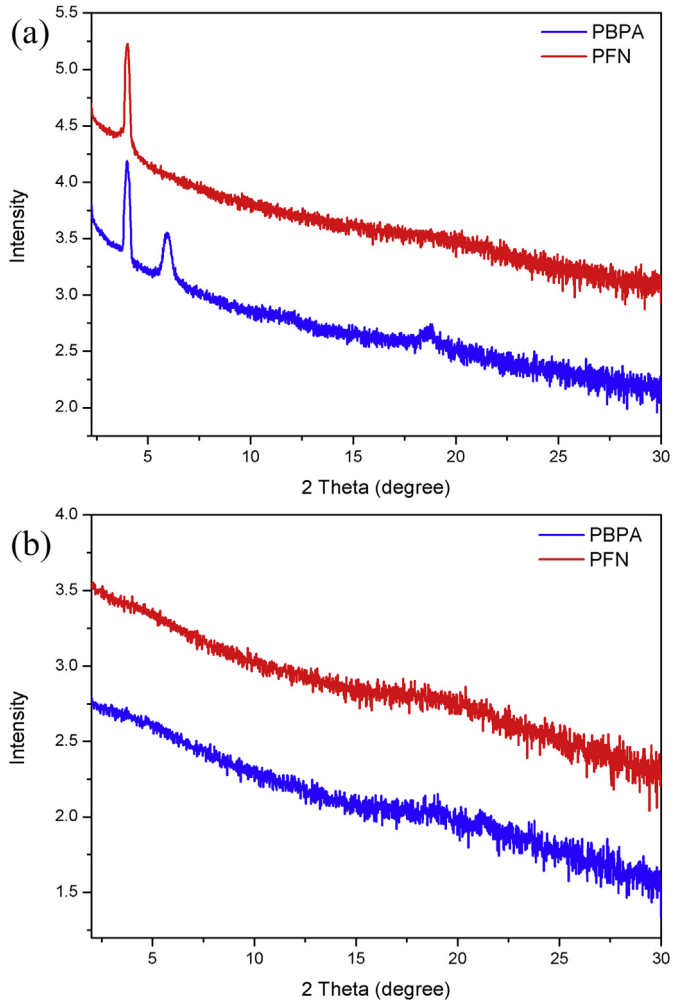

Fig. 4. X-ray diffraction pattern in thin films of PBPA and PFN a) out-of-plane and b) in-plane.

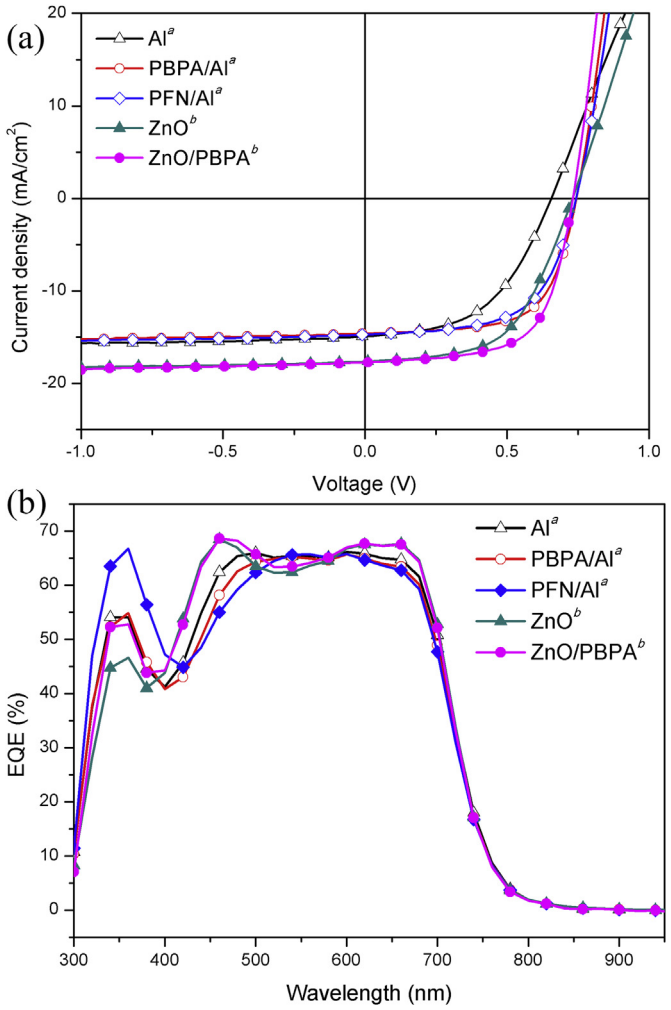

Fig. 5. a) *J*–*V* characteristics b) EQE spectra of the BHJ solar cells with the device ([a] Conventional device structure: ITO/PEDOT:PSS/PTB7:$PC_{71}BM$(1:1.5)/without or with interlayer/Al. [b] Inverted device structure: ITO/ZnO/without or with interlayer/PTB7:$PC_{71}BM$(1:1.5)/MoO_3/Ag.).

or a PFN solution formed a film (thickness of 5 nm) using the spin-coating method, and an Al electrode (100 nm) was deposited on top by evaporation through a shadow mask. We fabricated over 100 devices in order to confirm device reproducibility.

The OPV device without an interlayer exhibited V_{OC} of 0.65 V, J_{SC} of 14.9 mA/cm^2, FF of 50.0% and PCE of 4.9%, which is similar to the results of PTB7 device reported in the literature [16,32]. For a device with PFN, the V_{OC}, J_{SC}, FF and PCE were 0.73 V, 14.7 mA/cm^2, 60.7% and 6.6%, respectively. For a device with PBPA, the V_{OC}, J_{SC}, FF and PCE were 0.73 V, 14.6 mA/cm^2, 65.1% and 7.0%, respectively. The V_{OC} of the devices with either the PFN or the PBPA interlayer exhibited increased values. To verify the interfacial dipole moment of the PFN and PBPA, the surface potentials of active layers with and without interlayers are investigated through Scanning Kelvin probe microscopy (Fig. S7). It was noted that the potential of the films with interlayers are +200 mV higher than that of the film without interlayer. This suggests that the polar amino groups of PBPA and PFN contribute a powerful electrical field between the active layer and cathode interface [14,16].

The devices with an interlayer (PFN, PBPA) exhibited substantially increased FF values compared with the device without an interlayer. In particular, the FF of device with PBPA (65.1%) was higher than that with PFN (60.7%), which effected in the improved PCE of the device with PBPA (PFN 6.6% vs. PBPA 7.0%). The series resistance for the device with PBPA, as shown Table 2, was 6.9 Ω/cm^2, and the series resistance for the device with PFN was 8.0 Ω/cm^2, i.e., the series resistance of the PBPA layer exhibited a lower value compared with the PFN layer. This reduction of series resistance could grow the FF. Thus, the device with PBPA exhibited a higher FF than that of PFN because of the decrease of the series

Table 1
Optical & electrochemical properties of PBPA and PFN.

Polymer	Absorption, λ_{max} (nm)		E_{ox}^{onset} (V)	E_{HOMO} (eV)[c]	E_{LUMO} (eV)[d]	E_{opt} (eV)[e]	Hole mobility (cm^2/V s)[f]
	Solution[a]	Film[b]					
PBPA	301, 387	304, 384	0.94	−5.26	−2.29	2.96	2.86*10^{-5}
PFN	387	392	1.24	−5.57	−2.68	2.89	5.26*10^{-7}

[a] Absorption spectrum in $CHCl_3$ solution (10^{-6} M).
[b] Spin-coated thin film (50 nm).
[c] Calculated from the oxidation onset potentials under the assumption that the absolute energy level of Fc/Fc+ was −4.8 eV below a vacuum.
[d] HOMO − Eopt.
[e] Estimated from the onset of UV–vis absorption data of the thin film.
[f] Structure of the hole-only devices (ITO (170 nm)/PEDOT:PSS (40 nm)/PTB7:$PC_{71}BM$ (50 nm)/interlayer/MoO_3 (30 nm)/Al (100 nm)).

Table 2
Photovoltaic performance of the BHJ solar cells.

Device structure	V_{OC} (V)	J_{SC} (mA/cm^2)	FF (%)	PCE (%)	Rs (Ω/cm^2)	Rsh (Ω/cm^2)
Al	0.65	14.9	50.0	4.9 (4.9)[c]	13.9	533
PFN/Al[a]	0.73	14.7	60.7	6.6 (6.5)[c]	8.0	835
PBPA/Al[a]	0.73	14.6	65.1	7.0 (6.9)[c]	6.9	1044
ZnO[b]	0.73	17.6	55.1	7.2 (7.1)[c]	11.8	808
ZnO/PBPA[b]	0.73	17.7	63.6	8.3 (8.3)[c]	5.2	808

[a] Conventional device structure: ITO/PEDOT:PSS/PTB7:PC$_{71}$BM(1:1.5)/without or with interlayer/A.
[b] Inverted device structure: ITO/ZnO/without or with interlayer/PTB7:PC$_{71}$BM(1:1.5)/MoO$_3$/Ag.
[c] Average PCE value for five devices.

resistance resulting from the ordered orientation and packing of PBPA [6,19].

To confirm the preciseness of the cell performances, the external quantum efficiency (EQE) of each device was investigated, and the EQE curves are shown in Fig. 5(b). The short-circuit current density for the PFN- and PBPA-based devices obtained from the EQE data were both 13.5 mA/cm^2. Although it makes a little gap, the EQE data are similar with the cell current–density of AM 1.5 condition. In the case of PFN device, EQE showed increased intensity around 350–400 nm, which is because PFN absorb more photons around 350–400 nm as shown in UV result (Fig. 1b & Fig. S4)).

We also fabricated an inverted device as follows: ITO (170 nm)/ZnO (10 nm)/without or with PBPA (~5 nm)/active layer (50–80 nm)/MoO$_3$ (5 nm)/Ag (100 nm). For a device without PBPA, V_{OC}, J_{SC}, FF and PCE were 0.73 V, 17.6 mA/cm^2, 55.1% and 7.2%, respectively, which is similar to the results of inverted device reported in the literature [33]. The inverted OPV device with PBPA showed V_{OC} of 0.73 V, J_{SC} of 17.7 mA/cm^2, FF of 63.6% and PCE of 8.3%, which represent improved results over the PFN device reported in the literature [33].

3.5. Morphology and contact angle analysis

To analyze the torpology of the interlayer, atomic force microscopy (AFM) was investigated (Fig. 6). As shown in Fig. 6a, a smooth morphology was observed between PTB7 and PC$_{71}$BM, with a roughness of 0.9 nm. For the PBPA film on the top of the

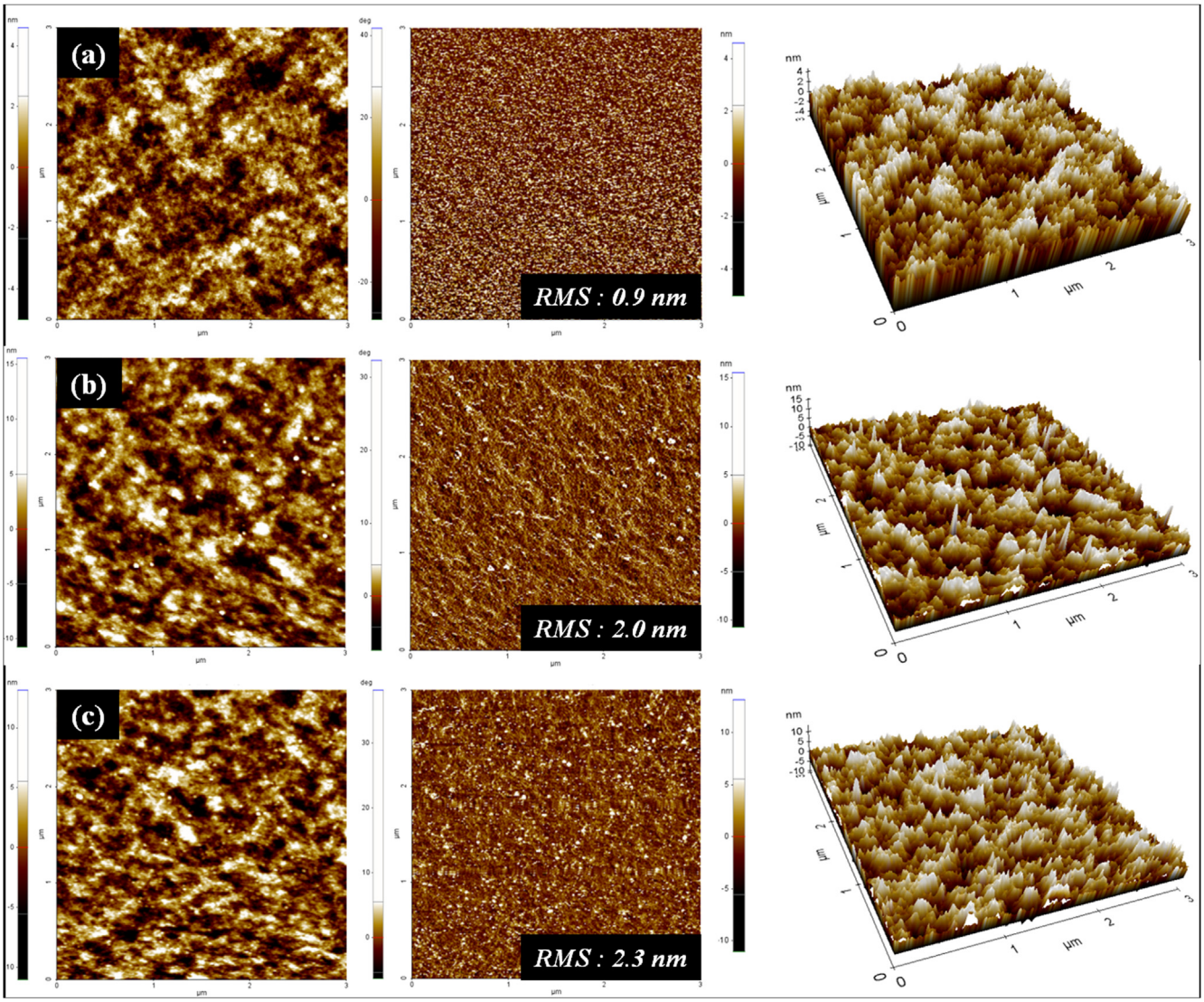

Fig. 6. Topographic AFM images of a) PTB7:PC$_{71}$BM film b) PTB7:PC$_{71}$BM/PBPA film c) PTB7:PC$_{71}$BM/PFN film (3 × 3 μm^2).

PTB7:$PC_{71}BM$ blend film (Fig. 6b)), a noticeable number of raised island-domains were observed. The roughness of the morphology of the PBPA film was 2.0 nm. In the case of the PFN film on the top of the PTB7:$PC_{71}BM$ blend film (Fig. 6c)), a number of raised island-domains were distributed over the film similar to the morphology of the PBPA film, with an increased roughness of 2.3 nm. The roughness of the PBPA film was lower than that of PFN. For the PBPA film, as shown in Fig. S8, the PBPA derivatives are assumed to form a flat packing due to its discotic structure, which may lead to a lower roughness compared with packing of PFN film. In contrast, in the case of the PFN film, the PFN derivatives are assumed to exhibit some aggregation, which may lead to increased roughness [14]. Thus, the PBPA film reduces the interfacial resistance compared with that of the PFN film due to its decreased roughness, which leads to the improved FF of the device with PBPA [33].

The water contact angle (Θ) of the surface of the device structures (ITO/PEDOT:PSS/PTB7:$PC_{71}BM$/without and with interlayer) was measured to explore the changes to the surface after the deposition of each interlayer. The contact angle of the PTB7:$PC_{71}BM$ layer was 99° due to its hydrophobic property. In contrast, the contact angle of the PTB7:$PC_{71}BM$/PFN and PTB7:$PC_{71}BM$/PBPA layers were 72° and 71°, respectively. These results suggest that deposition of an ionic component occurred on top of the organic surface [14]. The contact angle of the PTB7:$PC_{71}BM$/PBPA layer exhibited slightly lower angle compared with that of the PTB7:$PC_{71}BM$/PFN layer, which might be due to the planarity of the discotic structure (PBPA).

4. Conclusions

In this study, we synthesized novel alcohol/water-soluble discotic type pyrene derivatives (PBPA) using a simple synthesis process. PBPA exhibited good thermal stability and high solubility for organic and polar solvents. According to the CV measurement, the HOMO energy level of PBPA (−5.26 eV) is similar to that of PEDOT:PSS (−5.0 eV), which indicates that it could be used as the electron blocking and hole transport layers of OLEDs and OPVs. According to an XRD measurement, a huge fraction of the PBPA derivatives exhibit face-on orientation (electron transport direction) in regard of the substrate due to their discotic structure. The OPV device using PBPA exhibited improved characteristics compared with the devices using PFN (FF 65.1% vs. 60.7%, PCE 7.0% vs. 6.6%) due to the reduction of the interfacial resistance. In the case of a PBPA film on the top of the PTB7:$PC_{71}BM$ blend film, a noticeable number of raised island-domains were observed. the PBPA derivatives are assumed to form a flat packing due to their discotic structure. The inverted OPV device with PBPA showed V_{OC} of 0.73 V, J_{SC} of 17.7 mA/cm^2, FF of 63.6% and PCE of 8.3%, which represent improved results than PFN device.

Acknowledgments

This work was supported by the New & Renewable Energy Core Technology Program of the Korea Institute of Energy Technology Evaluation and Planning(KETEP) grant funded by the Ministry of Trade, Industry and Energy (MI, Korea) (No. 20133030000180).

Appendix A. Supplementary data

Supplementary data related to this article can be found at http://dx.doi.org/10.1016/j.dyepig.2014.08.007.

References

[1] Reineke S, Lindner F, Schwartz G, Seidler N, Walzer K, Lussem B, et al. White organic light-emitting diodes with fluorescent tube efficiency. Nature 2009;459:234–8.
[2] Wu H, Ying L, Yang W, Cao Y. Progress and perspective of polymer white light-emitting devices and materials. Chem Soc Rev 2009;38:3391–400.
[3] Gather MC, Köhnen A, Meerholz K. White organic light-emitting diodes. Adv Mater 2011;23:233–48.
[4] Earmme T, Ahmed E, Jenekhe SA. Solution-processed highly efficient blue phosphorescent polymer light-emitting diodes enabled by a new electron transport material. Adv Mater 2010;22:4744–8.
[5] Subramaniyan S, Xin H, Kim FS, Shoaee S, Durrant JR, Jenekhe SA. Effects of side chains on thiazolothiazole-based copolymer semiconductors for high performance solar cells. Adv Energy Mater 2011;1:854–60.
[6] Song H-J, Kim D-H, Lee E-J, Heo S-W, Lee J-Y, Moon D-K. Conjugated polymer consisting of quinacridone and benzothiadiazole as donor materials for organic photovoltaics: coplanar property of polymer backbone. Macromolecules 2012;45:7815–22.
[7] Krebs FC. Fabrication and processing of polymer solar cells: a review of printing and coating techniques. Sol Energy Mater Sol Cells 2009;93:394–412.
[8] Jiang J-M, Yang P-A, Hsieh T-H, Wei K-H. Crystalline low-band gap polymers comprising thiophene and 2,1,3-benzooxadiazole units for bulk heterojunction solar cells. Macromolecules 2011;44:9155–63.
[9] Jørgensen M, Carlé JE, Søndergaard RR, Lauritzen M, Dagnæs-Hansen NA, Byskov SL, et al. The state of organic solar cells—a meta analysis. Sol Energy Mater Sol Cells 2013;119:84–93.
[10] Liu Y, Larsen-Olsen TT, Zhao X, Andreasen B, Søndergaard RR, Helgesen M, et al. All polymer photovoltaics: from small inverted devices to large roll-to-roll coated and printed solar cells. Sol Energy Mater Sol Cells 2013;112:157–62.
[11] Huo L, Zhang S, Guo X, Xu F, Li Y, Hou J. Replacing alkoxy groups with alkylthienyl groups: a feasible approach to improve the properties of photovoltaic polymers. Angew Chem Int Ed 2011;50:9697–702.
[12] Dong S, Bao C, Tian H, Yan D, Geng Y, Wang F. ABAB-symmetric tetraalkyl titanyl phthalocyanines for solution processed organic field-effect transistors with mobility approaching 1 $cm^2 V^{-1} s^{-1}$. Adv Mater 2013;25:1165–9.
[13] Feng X, Marcon V, Pisula W, Hansen MR, Kirkpatrick J, Grozema F, et al. Towards high charge-carrier mobilities by rational design of the shape and periphery of discotics. Nat Mater 2009;8:421–6.
[14] Chen Y, Jiang Z, Gao M, Watkins SE, Lu P, Wang H, et al. Efficiency enhancement for bulk heterojunction photovoltaic cells via incorporation of alcohol soluble conjugated polymer interlayer. Appl Phys Lett 2012;100:203304.
[15] Kesters J, Ghoos T, Penxten H, Drijkoningen J, Vangerven T, Lyons DM, et al. Imidazolium-substituted polythiophenes as efficient electron transport materials improving photovoltaic performance. Adv Energy Mater 2013;3:1180–5.
[16] He Z, Zhong C, Huang X, Wong W-Y, Wu H, Chen L, et al. Simultaneous enhancement of open-circuit voltage, short-circuit current density, and fill factor in polymer solar cells. Adv Mater 2011;23:4636–43.
[17] He Z, Zhong C, Su S, Xu M, Wu H, Cao Y. Enhanced power-conversion efficiency in polymer solar cells using an inverted device structure. Nat Photonics 2012;6:591–5.
[18] Li Z, He G, Wan X, Liu Y, Zhou J, Long G, et al. Solution processable rhodanine-based small molecule organic photovoltaic cells with a power conversion efficiency of 6.1%. Adv Energy Mater 2012;2:74–7.
[19] Lee OP, Yiu AT, Beaujuge PM, Woo CH, Holcombe TW, Millstone JE, et al. Efficient small molecule bulk heterojunction solar cells with high fill factors via pyrene-directed molecular self-assembly. Adv Mater 2011;23:5359–63.
[20] Liu Y, Wan X, Wang F, Zhou J, Long G, Tian J, et al. High-performance solar cells using a solution-processed small molecule containing benzodithiophene unit. Adv Mater 2011;23:5387–91.
[21] Kyaw AKK, Wang DH, Gupta V, Zhang J, Chand S, Bazan GC, et al. Efficient solution-processed small-molecule solar cells with inverted structure. Adv Mater 2013;25:2397–402.
[22] Walker B, Kim C, Nguyen T-Q. Small molecule solution-processed bulk heterojunction solar cells†. Chem Mater 2010;23:470–82.
[23] Pho TV, Kim H, Seo JH, Heeger AJ, Wudl F. Quinacridone-based electron transport layers for enhanced performance in bulk-heterojunction solar cells. Adv Funct Mater 2011;21:4338–41.
[24] Takemoto K, Karasawa M, Kimura M. Solution-processed bulk-heterojunction solar cells containing self-organized disk-shaped donors. ACS Appl Mater Interfaces 2012;4:6289–94.
[25] Sienkowska MJ, Monobe H, Kaszynski P, Shimizu Y. Photoconductivity of liquid crystalline derivatives of pyrene and carbazole. J Mater Chem 2007;17:1392–8.
[26] Zhao B, Liu B, Png RQ, Zhang K, Lim KA, Luo J, et al. New discotic mesogens based on triphenylene-fused triazatruxenes: synthesis, physical properties, and self-assembly. Chem Mater 2009;22:435–49.
[27] Zhang Y, Zou J, Yip H-L, Chen K-S, Zeigler DF, Sun Y, et al. Indacenodithiophene and quinoxaline-based conjugated polymers for highly efficient polymer solar cells. Chem Mater 2011;23:2289–91.
[28] Fukuda M, Sawada K, Yoshino K. Synthesis of fusible and soluble conducting polyfluorene derivatives and their characteristics. J Polym Sci Part A Polym Chem 1993;31:2465–71.

[29] Hayer A, de Halleux V, Köhler A, El-Garoughy A, Meijer EW, Barberá J, et al. Highly fluorescent crystalline and liquid crystalline columnar phases of pyrene-based structures. J Phys Chem B 2006;110:7653–9.
[30] Osaka I, Akita M, Koganezawa T, Takimiya K. Quinacridone-based semiconducting polymers: implication of electronic structure and orientational order for charge transport property. Chem Mater 2012;24:1235–43.
[31] Song H-J, Kim D-H, Lee E-J, Moon D-K. Conjugated polymers consisting of quinacridone and quinoxaline as donor materials for organic photovoltaics: orientation and charge transfer properties of polymers formed by phenyl structures with a quinoxaline derivative. J Mater Chem A 2013;1:6010–20.
[32] Collins BA, Li Z, Tumbleston JR, Gann E, McNeill CR, Ade H. Absolute measurement of domain composition and nanoscale size distribution explains performance in PTB7:PC71BM solar cells. Adv Energy Mater 2013;3:65–74.
[33] Chang Y-M, Leu C-Y. Conjugated polyelectrolyte and zinc oxide stacked structure as an interlayer in highly efficient and stable organic photovoltaic cells. J Mater Chem A 2013;1:6446–51.